Solar RRL
www.solar-rrl.com

Role of Gd in Enhancing the Charge Carrier Mobility of Spray–Deposited $BiVO_4$ Photoanodes

Surassa Sriwichai, Rowshanak Irani, Fanxing Xi, Dennis Friedrich, Christian Höhn, Ibbi Y. Ahmet, Natda Wetchakun, and Fatwa F. Abdi**

The emergence of $BiVO_4$ as one of the most promising photoanodes for solar water splitting is largely driven by the success in dopant introduction and optimization to improve its photoelectrochemical performance. To this end, although less commonly used, several trivalent ions (e.g., In^{3+}, Gd^{3+}) that substitute Bi^{3+} have also been demonstrated to be effective dopants, which can increase the photocurrent of $BiVO_4$ photoanodes. However, the main factor behind such improvement is still unclear as various explanations were proposed in the literature. Herein, Gd^{3+} is introduced to substitute Bi^{3+} in spray-deposited $BiVO_4$ films, which enables up to a ~2-fold photocurrent increase. Further analysis suggests that Gd-doping enhances the carrier separation in $BiVO_4$ and does not affect the catalytic and optical properties. Indeed, time-resolved microwave conductivity measurements reveal that the carrier mobility of $BiVO_4$ is increased by 50% with the introduction of Gd, while the carrier lifetime is unaffected. This mobility increase is rationalized to be a result of a higher degree of monoclinic lattice distortion in Gd-doped $BiVO_4$, as evident from the X-ray diffraction and Raman spectroscopy data. Overall, these findings provide important insights into the nature and the underlying role of Gd in improving the performance of $BiVO_4$.

1. Introduction

Converting and storing solar energy as chemical energy through photoelectrochemical (PEC) water splitting is a promising approach to mitigate the global energy and environmental problems. The process utilizes semiconductor photoelectrodes to absorb sunlight and generate photoexcited electrons and holes, which drive the water oxidation or reduction reactions on their surfaces to form oxygen and hydrogen, respectively.[1,2] Metal oxides have been widely used as photoelectrode materials because of their general stability, multitude bandgap energies, relative abundance, and low synthesis cost.[3] Among the various metal oxides, bismuth vanadate ($BiVO_4$), particularly the monoclinic scheelite structure, has emerged as one of the most promising n-type oxide photoabsorbers for PEC water splitting.[4–6] Monoclinic $BiVO_4$ possesses a 2.4 eV bandgap, which allows visible light absorption, and favorable conduction and valence band positions for the water splitting reaction.[4–6] Nevertheless, the performance of unmodified $BiVO_4$ is limited by slow water oxidation kinetics[7] and poor carrier transport (i.e., mobility, lifetime) that limits the charge separation efficiency.[8,9] The latter is typically addressed by doping to tune the electrical properties of $BiVO_4$.[10] In particular, extrinsic doping, which is defined as the substitution or addition of a foreign element at the crystal lattice point of the host element,[11] has been widely applied to enhance the PEC performance of $BiVO_4$. For example, substituting V^{5+} with Mo^{6+},[12–14] W^{6+},[8,9,15,16] or both Mo^{6+} and W^{6+} simultaneously (i.e., codoping)[17–19] results in donor-doped $BiVO_4$ with increased carrier concentration. This enhances the electrical conductivity and, thus, the electron transport properties. Further enhancement of carrier separation has been reported by distributing the W^{6+} and Mo^{6+} composition throughout $BiVO_4$ (i.e., gradient doping).[20–22]

S. Sriwichai
PhD's Degree Program in Materials Science
Faculty of Science
Photocatalysts and 2D Materials Research Laboratory
Department of Physics and Materials Science
Chiang Mai University
Chiang Mai 50200, Thailand

The ORCID identification number(s) for the author(s) of this article can be found under https://doi.org/10.1002/solr.202100268.

Dr. R. Irani, Dr. F. Xi, Dr. D. Friedrich, C. Höhn, Dr. I. Y. Ahmet, Dr. F. F. Abdi
Institute for Solar Fuels
Helmholtz–Zentrum Berlin für Materialien und Energie GmbH
Hahn–Meitner–Platz 1, Berlin 14109, Germany
E-mail: fatwa.abdi@helmholtz-berlin.de

Dr. N. Wetchakun
Photocatalysts and 2D Materials Research Laboratory
Department of Physics and Materials Science
Faculty of Science
Center of Excellence in Materials Science and Technology
Chiang Mai University
Chiang Mai 50200, Thailand
E-mail: natda.we@cmu.ac.th

DOI: 10.1002/solr.202100268

The substitution of Bi^{3+} in $BiVO_4$ with trivalent ions has also been reported. Interestingly, in contrast to the Mo or W doping described earlier, the isovalent nature of the dopants, in this case, is not expected to directly modify the carrier concentration of $BiVO_4$. Other roles have therefore been proposed. For example, the incorporation of In^{3+} in $BiVO_4$ was reported to inhibit surface charge recombination due to surface state passivation.[23] Govindaraju et al. evaluated several lanthanide ions (La, Ce, Sm, and Yb) as dopants in $BiVO_4$ and reported multiple roles.[24] Doping with La and Ce was found to decrease the PEC performance due to an increase of the effective mass of carriers (as shown from density functional theory, DFT) and/or an introduction of a midgap state that acts as recombination center. Meanwhile, Sm and Yb doping, despite the main 3+ oxidation state, indirectly increased the carrier concentration in $BiVO_4$ because of the coexistence of oxygen vacancies that introduced shallow donor states and enhanced the PEC performance. Gd has also been reported as an effective dopant in $BiVO_4$ photocatalyst powders, and higher photocatalytic activity for the degradation of methylene blue and rhodamine B was reported.[25,26] It was suggested that the half-filled 4*f* electronic configuration of Gd^{3+} ions on the surface of $BiVO_4$ is beneficial for trapping charges and enhancing charge transfer for the catalytic reactions. An optimal Gd-doping concentration also simultaneously enhances the activity, selectivity, and stability of $BiVO_4$ for the water oxidation to H_2O_2 production.[27] Newhouse et al. showed that Gd doping modified the monoclinic distortion in the lattice of $BiVO_4$, which was expected to decrease the hole effective mass as shown by their DFT results.[28] Further improvement was demonstrated by combining Gd doping with an additional transition metal (W or Mo) as electron donor and H_2 annealing to improve the carrier lifetime.[29] Overall, various assignments have been proposed, which demonstrates that the main role of trivalent dopants in $BiVO_4$, especially Gd, is still not clear. To unravel this, further investigation on the influence of trivalent ion doping on the photoelectrochemical properties (e.g., carrier transport and catalytic activity) of $BiVO_4$ is still needed.

In this study, we fabricated Gd-doped and (Gd,W)-co-doped $BiVO_4$ thin film photoanodes using spray pyrolysis, which demonstrate up to twice as high photocurrents as compared to that of pristine $BiVO_4$. This photocurrent enhancement is found to be a result of a higher charge separation efficiency, not catalytic efficiency. In contrast to W doping,[8] Gd doping enhances the carrier mobility while maintaining the relatively long carrier lifetime in $BiVO_4$ as measured by time-resolved microwave conductivity (TRMC). To the best of our knowledge, this is the first direct experimental study that correlates Gd doping in $BiVO_4$ to the modulation of its carrier transport properties. Further effects of Gd doping on the optical, surface chemical composition, morphological, and structural properties of $BiVO_4$ will also be discussed.

2. Results and Discussion

2.1. Photoelectrochemical and Optoelectronic Properties of Gd–Doped $BiVO_4$

As slow surface reaction kinetics (i.e., slow hole transfer across the semiconductor/electrolyte interface) have been shown to limit the photocurrent of $BiVO_4$,[7] sodium sulfite (Na_2SO_3) was added into the electrolyte in this study as hole scavenger to eliminate any surface catalytic limitations.[30] Deposition of various cocatalysts (e.g., NiFeOOH and CoP_i) has been demonstrated to overcome this limitation in a hole-scavenger-free electrolyte,[7,31,32] but this is not the focus of our work. The AM 1.5 photocurrent–voltage curves for $BiVO_4$ and 1% Gd–$BiVO_4$ films in 2 M KP_i with and without 0.5 M Na_2SO_3 are shown in **Figure 1**. In both electrolytes, 1% Gd doping results in a significantly higher photocurrent and a cathodic shift of the onset potential of $BiVO_4$; the effect is more pronounced in the presence of hole scavengers. The Gd concentration was also varied up to 3% ($Bi_{1-x}Gd_xVO_4$; $x = 0$, 0.005, 0.01, 0.02, and 0.03). The crystal structure of all these samples was found to be monoclinic scheelite $BiVO_4$, which will be shown and discussed in a later section of the manuscript. The AM 1.5 photocurrents at 1.23 V_{RHE} are plotted as a function of the Gd concentration, as shown in **Figure 2** and Figure S1a, Supporting Information. All Gd-doped $BiVO_4$ films show higher photocurrents at 1.23 V_{RHE} than the undoped film, and 1% is found to be the optimum Gd concentration. The photocurrent of $BiVO_4$ and 1% Gd–$BiVO_4$ at 1.23 V_{RHE} is ≈1.8 and 3.4 mA cm^{-2}, respectively. This approximately twofold photocurrent improvement underlines the effectiveness of Gd doping in $BiVO_4$. We also note that the photocurrent of the 1% Gd–$BiVO_4$ film is of the same order as those reported for spray-pyrolyzed gradient-doped W–$BiVO_4$ films,[20,21] which is among the highest for nonnanostructured $BiVO_4$.

We then combined Gd doping with W doping (i.e., codoping) because W has been widely used as a donor dopant to improve the electrical conductivity of $BiVO_4$.[8,9,15,16] The AM 1.5 photocurrents of 1% W-doped $BiVO_4$ films with varying concentrations of Gd are shown in Figure S1b,c, Supporting Information (the synthesis of W-doped $BiVO_4$ and (Gd,W)-codoped $BiVO_4$ films is described in Supporting Note S1, Supporting Information). Gd doping is also effective in improving the photocurrent of W-doped $BiVO_4$ and the same optimum concentration of 1% Gd was found. Surprisingly, the photocurrents of the (Gd,W)-codoped $BiVO_4$ films are lower than those of Gd-doped films. This observation is in contrast to the case of (Gd, Mo)-codoped $BiVO_4$ films, as reported by Newhouse et al.[28] The

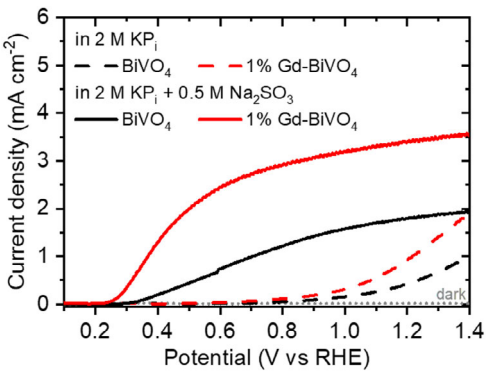

Figure 1. Photocurrent–voltage curves of $BiVO_4$ (black) and 1% Gd—$BiVO_4$ (red) in 2 M KP_i with (solid lines) and without 0.5 M Na_2SO_3 as a hole scavenger (dashed lines) under backside AM 1.5 illumination. The dark current is shown by the dotted gray line.

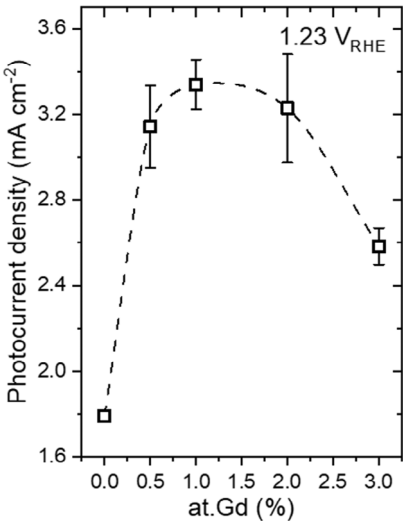

Figure 2. AM 1.5 photocurrent at 1.23 V_{RHE} under backside illumination for $BiVO_4$ films with various Gd-dopant concentrations. The error bars represent the variation from measurements of three duplicate samples. The photocurrent–voltage curves for each Gd concentration are shown in Figure S1a, Supporting Information.

photocurrents of (Gd,Mo)-codoped $BiVO_4$ was enhanced when compared to the single doping with Gd or Mo, which was attributed to the lower hole effective mass. More recently, they also reported that an enhancement can also be obtained by codoping with Gd and W, although not as large as codoping with Gd and Mo.[29] We speculate that the reason for this difference is related to the difference in the preparation method. First, inkjet printing was used in their study versus spray pyrolysis in our study. The range of the dopant concentration investigated is also different. Finally, Newhouse et al. maintained the stoichiometry of Bi and V (i.e., Bi:V = 1:1),[29] but in this study we adjust the Bi and V precursor concentration to accommodate for the W and Gd dopants, such that (Bi + Gd):(V + W) = 1:1. Although undoubtedly interesting, it is clear that codoping introduces more complexity toward understanding the main role of Gd, which is beyond the scope of the current work. Throughout the remainder of this study, we therefore focus only on Gd-doped $BiVO_4$ films, since monodoping $BiVO_4$ with Gd has been shown unambiguously to be effective in various reports.

To investigate the cause behind the photocurrent improvement, we calculated the catalytic efficiency (also often called "charge injection efficiency") from the photocurrent–voltage curves in the absence and presence of Na_2SO_3 as hole scavengers in the electrolyte. The method has been described in previous reports,[16,33,34] and the determination of catalytic efficiency is explained in Supporting Note S2, Supporting Information. The calculated catalytic efficiencies for $BiVO_4$ and 1% Gd–$BiVO_4$ are shown in Figure S2, Supporting Information. At potentials higher than ≈1.1 V_{RHE}, a slight increase of the catalytic efficiency was observed with 1% Gd doping. However, this enhancement is minor compared to the photocurrent increase, suggesting that bulk modifications are the main reason instead.

To investigate the optical absorption of the films, UV–vis spectroscopy measurements were performed on the undoped $BiVO_4$ and 1% Gd–$BiVO_4$ films deposited on quartz substrates. The UV–vis absorption spectra and the photographs of the measured samples are shown in **Figure 3**a. No significant difference in the absorptance can be observed; the 1% Gd–$BiVO_4$ shows slightly lower absorptance at wavelengths lower than 475 nm, but such a difference is within the sample-to-sample variation. The optical bandgap energy (E_g) can be obtained by the Tauc equation[35]

$$(\alpha h\nu)^{1/n} = A(h\nu - E_g) \tag{1}$$

where α is the absorption coefficient, h is Planck's constant, ν is the light frequency, A is the proportional constant, and n is 1/2 or 2 for direct or indirect allowed transition, respectively. For Tauc analysis in this study, the α in Equation (1) was approximated using the Kubelka–Munk function (F) of the film's transflectance (TR):[36]

$$F = \frac{(1 - \mathrm{TR})^2}{2\mathrm{TR}} \tag{2}$$

The Tauc plots for direct and indirect bandgaps are shown in Figure 3b,c, respectively. Again, no changes can be observed between the direct or indirect bandgaps of $BiVO_4$ and 1% Gd–$BiVO_4$, indicating that Gd incorporation does not affect the optical properties of our spray-deposited $BiVO_4$.

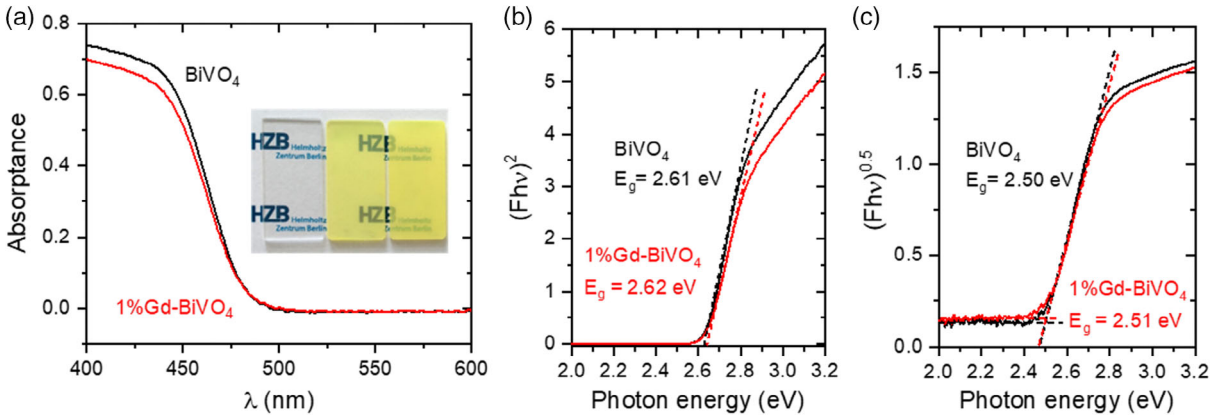

Figure 3. a) Optical absorption of $BiVO_4$ and 1% Gd—$BiVO_4$ films on quartz. The inset shows photographs of the (left to right) blank quartz substrate, $BiVO_4$, and 1% Gd—$BiVO_4$ on quartz. Tauc plots for b) direct and c) indirect bandgap analysis of $BiVO_4$ and 1% Gd—$BiVO_4$ films.

The fact that no significant catalytic or absorption changes could be observed upon Gd doping suggests that the improved photoelectrochemical properties are related to the enhancement of the charge separation efficiency. A possible factor that may increase the charge separation efficiency is an increase of conductivity due to higher carrier concentration. This is, however, unlikely to be the case as Gd is an isovalent dopant and we will discuss later that the process of introducing Gd into our $BiVO_4$ should not be compensated for with any electronic or ionic defects. We therefore evaluate the charge transport properties of both undoped and 1% Gd–$BiVO_4$ by performing TRMC measurements. Briefly, both films are excited with a nanosecond laser pulse (photon energy $h\nu >$ bandgap), resulting in the formation of free electrons and holes, which are then detected as a change in the microwave power reflected from the samples. This change corresponds to the change of photoconductance (ΔG), which is then monitored as a function of time (i.e., transient). The relative comparison of the peak transient can be used to evaluate the charge carrier mobility, and the charge carrier lifetime can be obtained from the transient decay.[35,37]

Figure 4a shows the transient photoconductance responses, normalized to the absorption (F_A) and photon flux (I_0), for the undoped and 1% Gd–$BiVO_4$ films. The measurements were performed under backside 350 nm laser pulse illumination (i.e., $h\nu \approx 3.5$ eV $> E_g$ of $BiVO_4$), and the I_0 was 4.3×10^{13} pulse^{-1} cm^{-2}. Upon Gd doping, the peak $\Delta G/(F_A I_0)$ transient increases by a factor of 1.5, which indicates an improvement of the charge carrier mobility. In contrast, the transient decay does not seem to be affected. This can be seen clearly from Figure 4b, in which the transient photoconductance of each sample is normalized against the peak value (i.e., $\Delta G/\Delta G_{max}$). Both transients overlap with each other, which indicates that the charge carrier lifetime of $BiVO_4$ is unaffected by Gd doping. This also suggests that the charge transport mechanism is likely to be the same in both films. Similar effects to the transient peak and decay can also be observed for other excitation wavelengths (see Figure S3, Supporting Information). Overall, the higher mobility and constant lifetime with Gd doping result in an extended charge carrier diffusion length, which can explain the enhanced charge separation and observed photocurrent improvement.

2.2. Influence of Gd Incorporation on the Chemical, Morphological, and Structural Nature of Spray–Deposited $BiVO_4$

We now investigate the underlying chemical, morphological, and structural changes associated with the introduction of Gd into our $BiVO_4$, which may be responsible for the improvement of the carrier mobility. The presence of Gd in the Gd-doped $BiVO_4$ films is first confirmed by performing X-ray photoelectron spectroscopy (XPS). Bi 4*f*, V 2*p*, O 1*s*, and Gd 4*d* core-level spectra of undoped $BiVO_4$, 1% Gd–$BiVO_4$, and 3% Gd–$BiVO_4$ films are shown in Figure 4,5, Supporting Information. Although the Gd 4*d* spectra are rather noisy due to the low concentration, Gd can be detected in the Gd-doped films, and the introduction of Gd does not introduce any changes to the Bi 4*f*, V 2*p*, or O 1*s* spectra. This is not surprising, since the isovalent substitution of Bi with Gd (i.e., $Gd_{Bi}^{\times}$) does not require any ionic or electronic compensations. Based on the XPS spectra, we found that the Gd atomic concentration in the films matches relatively well with the amount introduced into the spray precursor solution. A Gd atomic concentration of 1.3% and 2.9% was calculated for the 1% Gd–$BiVO_4$ and 3% Gd–$BiVO_4$ films, respectively.

The Gd incorporation was then evaluated for any influences in the morphology of the $BiVO_4$ films. **Figure 5** shows the top-view scanning electron micrographs of undoped $BiVO_4$, 1% Gd–$BiVO_4$, and 3% Gd–$BiVO_4$ films. Similar interconnected irregular grain features can be observed from all films, and the grain size is slightly increased with increasing Gd doping concentrations: 183 ± 58 nm for undoped $BiVO_4$, 218 ± 57 nm for 1% Gd–$BiVO_4$, and 289 ± 96 nm for 3% Gd–$BiVO_4$. An increase in grain size would reduce the amount of grain boundary scattering, and this has been demonstrated to be the cause for an increase in charge carrier mobility and photocurrent.[38,39] However, the continuous increase of grain size with increasing Gd concentration does not agree with the presence of the photocurrent maximum for the 1% Gd concentration. This suggests that the cause behind the enhanced charge carrier mobility and photoelectrochemical performance in our films is unlikely to be related to the morphology change.

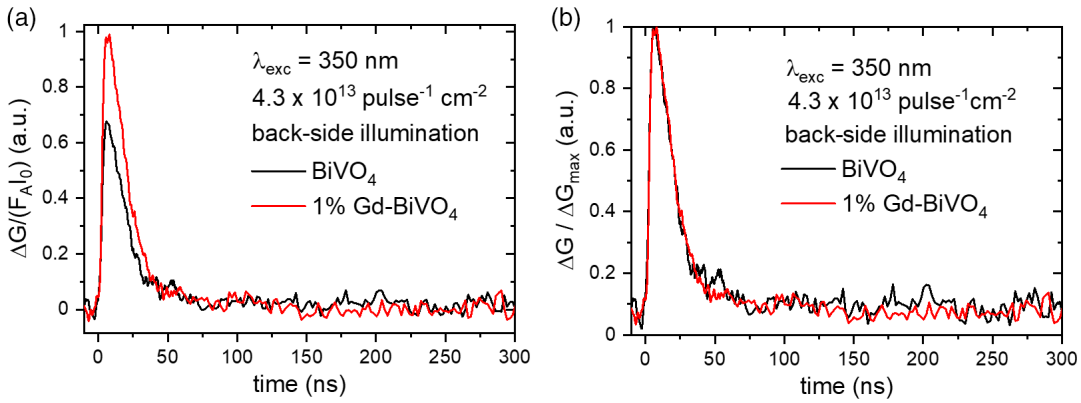

Figure 4. a) Transient photoconductance, $\Delta G/(F_A I_0)$, signals and b) normalized photoconductance, $\Delta G/\Delta G_{max}$, recorded for $BiVO_4$ (black) and 1% Gd—$BiVO_4$ (red) under backside 350 nm laser pulse illumination with a photon flux, I_0, of 4.3×10^{13} pulse^{-1} cm^{-2}.

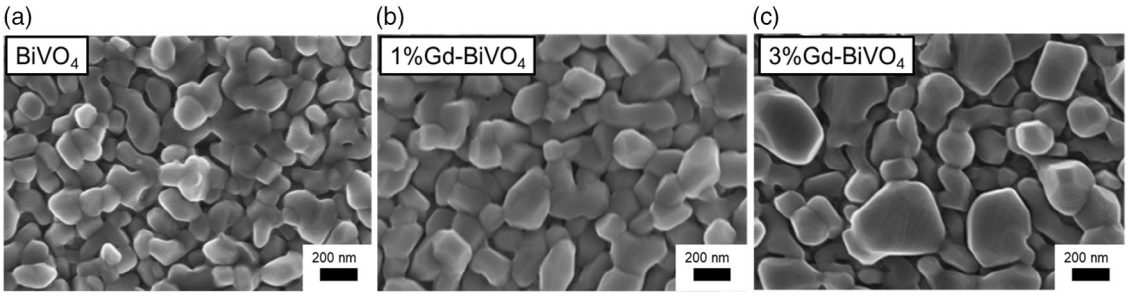

Figure 5. Top-view scanning electron micrographs for a) $BiVO_4$, b) 1% Gd—$BiVO_4$, and c) 3% Gd—$BiVO_4$ films deposited on FTO substrates.

Finally, the influence of Gd doping on the crystal structure of $BiVO_4$ films is investigated by performing X-ray diffraction and Raman spectroscopy measurements. **Figure 6**a shows the grazing incidence X-ray diffraction patterns for undoped $BiVO_4$, 1% Gd–$BiVO_4$, and 3% Gd–$BiVO_4$ films. Reference diffraction patterns of monoclinic and tetragonal scheelite $BiVO_4$ are also shown. The distinction between the tetragonal and monoclinic scheelite is that the local environments of V and Bi ions are more notably distorted in the monoclinic versus tetragonal structure. As a result, two different V—O bond lengths are present in monoclinic scheelite, whereas there is only one V—O bond length in tetragonal scheelite.[40] All our $BiVO_4$ films show diffraction peaks that match well with those of monoclinic scheelite $BiVO_4$ without any impurity phases. In contrast to other reports,[26,27] we do not observe a transition from monoclinic to tetragonal scheelite in our $BiVO_4$ films with Gd doping, which will be discussed later. Figure S6, Supporting Information, shows that the $(\bar{1}21)$ peak position slightly shifts to a higher 2θ angle upon Gd doping. This shift is consistent with the notion of substituting Bi^{3+} ions (ionic radius = 1.17 Å) with Gd^{3+} ions (1.05 Å),[41] which has also been shown in a report of Gd-doped Bi_2O_3 powder.[42]

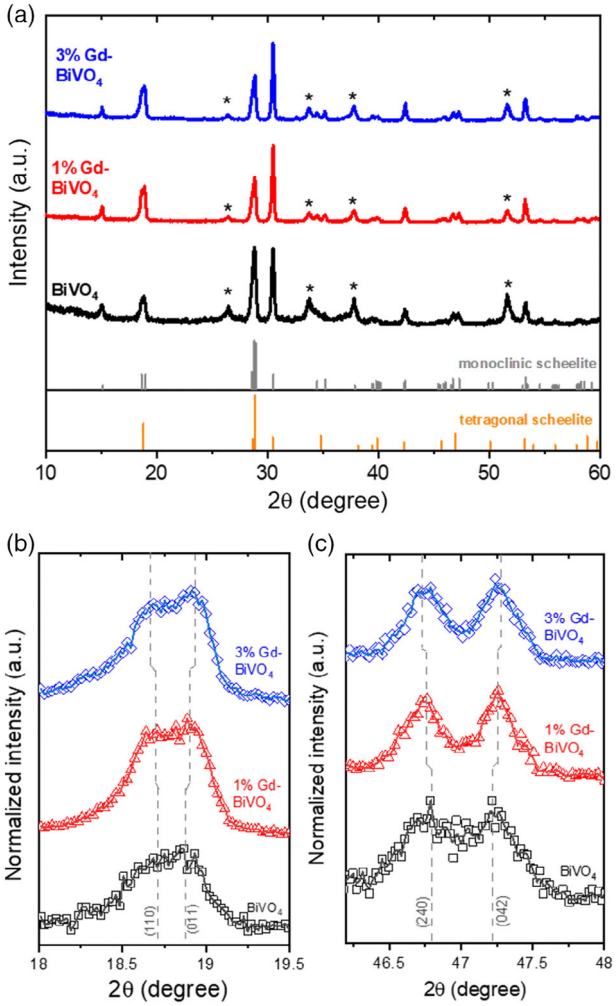

Figure 6. a) X-ray diffractograms for undoped $BiVO_4$, 1% Gd—$BiVO_4$, and 3% Gd—$BiVO_4$ films on FTO substrates. The FTO peaks are indicated with a star (*). The characteristic peak splitting of monoclinic scheelite is shown in the range of b) $2\theta = 18°–19.5°$ and c) $2\theta = 46°–48°$. The dashed vertical lines with offset are shown to highlight the further splitting of the peaks with Gd doping in our $BiVO_4$.

A closer look at the {110} and {240} X-ray diffraction peaks (Figure 6b,c) reveals that the monoclinic peak splits further apart with higher Gd concentration, suggesting increased distortion of the crystal lattice with Gd incorporation in our films. To confirm this observation, Raman spectroscopy was performed to shed light on the short-range order and the V—O bond lengths in our films. The Raman spectra are indicated in **Figure 7** and the positions of the assigned Raman bands are given in Table S1, Supporting Information. All the Raman peaks agree with those described in previous reports on monoclinic scheelite $BiVO_4$.[28,29,43,44] Consistent with the XRD results, the structural change from monoclinic scheelite to tetragonal scheelite, which can be identified by the merging of peaks belonging to the symmetric bending mode $\delta_s(VO_4^{3-})$ and asymmetric bending mode $\delta_{as}(VO_4^{3-})$ into one,[28,29,44] is not observed with Gd incorporation into our films (see Figure 7b). Instead, as the discontinuity in the dashed lines shows, $\delta_s(VO_4^{3-})$ and $\delta_{as}(VO_4^{3-})$ slightly shift to higher wavenumber with Gd incorporation. The same shift to higher wavenumber is also observed for the symmetric and asymmetric V—O stretching mode (ν_s(V—O) and ν_{as}(V—O); see Figure 7c). Based on the empirical relationship reported by Hardcastle et al.,[45,46] the V—O bond lengths can be calculated using the following equation

$$\nu = 21349 \exp(-1.9176R) \quad (3)$$

where is the Raman stretching frequency in cm^{-1} (symmetric and asymmetric) and R is the V—O bond length in angstrom.

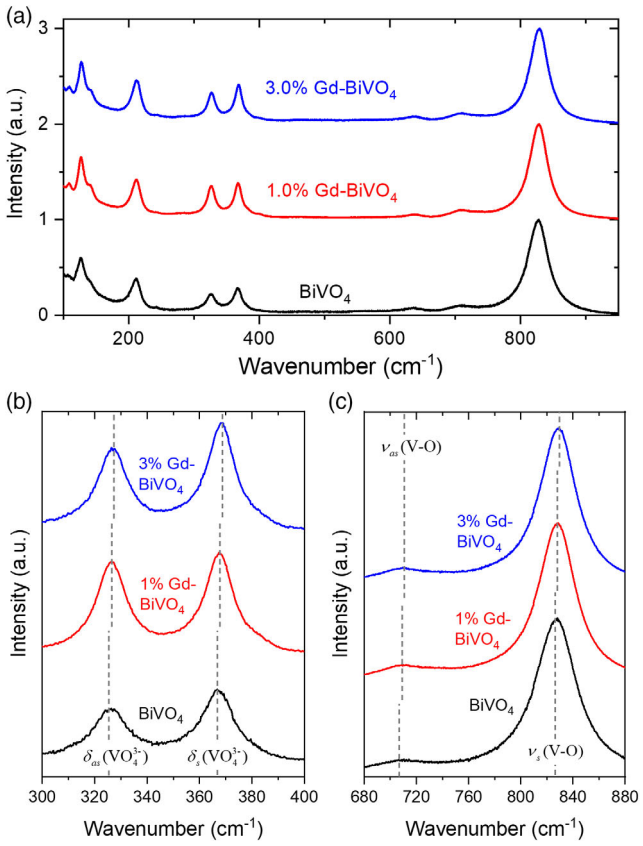

Figure 7. a) Raman spectra of undoped $BiVO_4$, 1% Gd—$BiVO_4$, and 3% Gd—$BiVO_4$. Specific regions depicting the b) bending modes and c) stretching modes are also shown. The dashed lines in (b) and (c) and their discontinuity highlight the shift of the peaks toward higher wavenumber.

The calculated V—O bond lengths are tabulated in Table S1, Supporting Information. The values obtained (≈1.69 and ≈1.77 Å) are in very good agreement with those observed previously for $BiVO_4$,[40,47] and the incorporation of Gd into our $BiVO_4$ films induces a slight decrease in the V—O bond length. Indeed, decreased V—O bond length has been shown to correlate with the increased photocatalytic performance of $BiVO_4$.[48,49] It was reported that a shorter V—O bond length in the VO_4^{3-} tetrahedron provides a stronger packed structure and a greater degree of distortion of the VO_4^{3-} tetrahedron, which correlates with the distortion of the Bi—O polyhedron by the lone-pair electron of Bi^{3+} in the local structure of $BiVO_4$. A higher degree of distortion of the local structure therefore increases the overlap between the Bi 6*s* and O 2*p* orbitals, which enhances the photogenerated hole mobility and the overall photocatalytic activity for O_2 evolution.[48,49] We therefore attribute the same effect to our Gd-doped $BiVO_4$; the shorter V—O bond length in the VO_4^{3-} tetrahedron provides a higher degree of local structural distortion in monoclinic scheelite $BiVO_4$. The optimal degree of distortion is obtained for the 1% Gd–$BiVO_4$ film, which enhances the charge carrier mobility as observed in our TRMC measurements as well as the resulting photoelectrochemical performance.

Finally, we discuss the possible reason for the difference in observation between our Gd-doped $BiVO_4$ films and those reported in the literature.[26,28,29] Whereas reports in the literature suggest that Gd incorporation induces a transition from monoclinic to tetragonal, we instead show that this is not the case in our spray-deposited $BiVO_4$ films. One possible reason is that we maintain a relatively low Gd dopant concentration in our study. Another possible reason, which we believe is more likely, is related to the different synthesis procedures, specifically in the way that stoichiometry is maintained in the resulting Gd-doped $BiVO_4$. In studies reported in the literature, a Bi:V ratio of 1:1 was maintained in the Gd-doped films. This can be represented by a dissolution reaction of Gd_2O_3 into the lattice of $BiVO_4$, as shown in the Kröger–Vink notation[50]

$$Gd_2O_3 \xrightarrow{2BiVO_4} 2Gd_{Bi}^{\times} + 2V_V^{/////} + 3O_O^{\times} + 5V_O^{\cdot\cdot} \quad (4)$$

The introduction of Gd is compensated for by the formation of vanadium and oxygen vacancies ($V_V^{/////}$ and $V_O^{\cdot\cdot}$). These vacancies may affect the crystal structure as well as the photoelectrochemical performance of the resulting $BiVO_4$. An alternative defect chemical reaction can be written in the presence of excess oxygen during dissolution, but the formation of vanadium vacancies remains

$$Gd_2O_3 + \frac{5}{2}O_2(g) + 10e^{/} \xrightarrow{2BiVO_4} 2Gd_{Bi}^{\times} + 2V_V^{/////} + 8O_O^{\times} \quad (5)$$

In our study, however, we did not maintain the Bi:V ratio to be 1:1. Instead, we kept the (Bi+Gd):V ratio as 1:1. This is typically written as a codoping process in the defect chemical equation; i.e., excess V was introduced along with the Gd-doping

$$Gd_2O_3 + V_2O_5 \xrightarrow{2BiVO_4} 2Gd_{Bi}^{\times} + 2V_V^{\times} + 8O_O^{\times} \quad (6)$$

As shown previously, using this method, the introduction of Gd as dopant is not accompanied by the formation of any vacancies. We therefore speculate that the formation of these vacancies is the driving force for the transition from the monoclinic to tetragonal phase shown in the literature. Overall, this comparison underlines the importance of controlling the stoichiometry in the doping process of complex metal oxides.

3. Conclusion

In summary, we successfully introduced Gd as dopants in spray-pyrolyzed $BiVO_4$ films. Gd doping enhances the AM 1.5 photocurrent density, and 1 at% Gd is found to be the optimal concentration, resulting in a twofold improvement of the photocurrent density. Time-resolved microwave conductivity data suggest that the photocurrent improvement is caused by the increase of charge carrier mobility, which in turn results in better charge separation. Detailed structural analysis of the films via X-ray diffraction and Raman spectroscopy measurements reveal that Gd doping introduces further distortion of the monoclinic lattice by the reduction of the V—O bond lengths. This distortion has been correlated to the increase of photogenerated hole mobility,[48,49] which is consistent with our TRMC results. Finally, by

comparing these findings with previous literature reports on Gd-doped $BiVO_4$, we propose alternative defect reactions associated with introducing Gd into monoclinic $BiVO_4$, and highlight the delicate nature of doping in ternary metal oxides.

4. Experimental Section

Spray Pyrolysis of $BiVO_4$ and Gd–Doped $BiVO_4$ Thin Films: $BiVO_4$ and Gd-doped $BiVO_4$ film photoanodes were prepared by spray pyrolysis, which is a low-cost, facile, and scalable process for depositing $BiVO_4$ thin films.[51,52] The $BiVO_4$ precursor solution was prepared by dissolving 0.8 mmol of $Bi(NO_3)_3{\cdot}5H_2O$ (98%, Sigma–Aldrich) in acetic acid and dissolving 0.8 mmol $VO(AcAc)_2$ (99%, Alfa Aesar) in absolute ethanol. To prevent premature oxidation by trace amounts of water, triethyl orthoformate (TEOF, 98%, Fluka Analytical) was added to the Bi and V solution (TEOF reacts with water to form ethyl formate and ethanol).[53] The V solution was then added to the Bi solution, and the mixture was diluted with excess absolute ethanol to end up with a final precursor concentration of 4 mM. The ratio of acetic acid to ethanol in the final solution was 1:9. For the deposition of 0.5–3 at% Gd-doped $BiVO_4$ ($Bi_{1-x}Gd_xVO_4$; $x = 0.005$, 0.01, 0.02, and 0.03), $Gd(NO_3)_3{\cdot}6H_2O$ (99%, Sigma–Aldrich) was used as the Gd precursors. Varying amounts of $Gd(NO_3)_3{\cdot}6H_2O$ were added to the Bi precursor solution. The V solution was then added to the (Bi+Gd) solution, resulting in a mixture containing (Bi+Gd):V in a 1:1 ratio. TEC 7 FTO-coated glass or quartz was used as the substrate, which was cleaned by three successive 15 min ultrasonic cleaning treatments in acetone, absolute ethanol, and deionized water. The substrate temperature during spray was maintained at 450 °C. The spray deposition was carried out using an automated spray setup with a Quickmist air atomizing spray nozzle (1/4QMJAU–NC + SUQR-200) driven by an overpressure of nitrogen gas. The nozzle-to-substrate distance was kept at 20 cm. Each spray cycle consisted of 5 s of spray time and 55 s of delay time to allow solvent evaporation. The precursor solution (180 mL) was sprayed onto the heated substrate with a spray rate of 1–1.5 mL per spray cycle. For films deposited on FTO-coated glass substrates, a thin SnO_2 layer was spray deposited onto the FTO substrate prior to the $BiVO_4$ deposition using 5 mL of 0.1 M $SnCl_4$ solution in ethyl acetate, to prevent the recombination of electrons and holes at the FTO/$BiVO_4$ interface according to the previously reported procedure.[9] As a final step, all of the samples were annealed at 450 °C for 2 h with a heating rate of 5 °C min^{-1} in air to further improve the crystallinity.

Characterization: UV–vis spectroscopy was performed using a Lambda 950 spectrophotometer (Perkin Elmer) equipped with an integrating sphere. TRMC measurements were performed using a home-built setup described in more detail previously.[8,37,54] In short, the $BiVO_4$% and 1% Gd–$BiVO_4$ films deposited on quartz were placed in a microwave cavity cell. During the measurements, a change in the microwave power was reflected by the cavity upon nanosecond excitation pulses of a diode-pumped Q-switched Nd:YAG laser (coupled with a wavelength tunable optical parametric oscillator, OPO) at a wavelength of 350, 410, and 450 nm. X-band microwaves were generated by a voltage-controlled oscillator (SiversIMA VO3262X). XPS was conducted with a monochromatic Al Kα source (1486.74 eV, SPECS FOCUS 500) and a hemispherical analyzer (SPECS PHOIBOS 100) to study the composition and the oxidation state of the elements. The data were calibrated using the carbon peak at 284.5 eV. Field-emission scanning electron microscopy (FESEM) was performed using a LEO GEMINI 1530 instrument from ZEISS operated with an acceleration voltage of 5 kV. The crystal structure of all samples was studied by X-ray diffraction using a Bruker D8 diffractometer with a Cu Kα radiation ($\lambda = 1.54184$ Å) at 40 kV and 40 mA. Grazing incidence configuration was used with an incident angle of 1.0°. The diffraction patterns were recorded in the range of $2\theta = 10°$–$60°$ at a step size of 0.0225°. Raman spectroscopy was performed using a Horiba HR800 spectrometer equipped with a HeNe laser (λ = 632.8 nm) as the excitation source.

Photoelectrochemical Measurements: Photoelectrochemical measurements were performed in a three-electrode configuration at room temperature, with a platinum wire as the counter electrode, an Ag/AgCl electrode (XR300, saturated KCl and AgCl solution, Radiometer Analytical) as the reference electrode, and the $BiVO_4$ as the working electrode (surface area 0.24 cm^2). Electrical contact to the $BiVO_4$ films was provided by a copper wire as well as a conducting electrical tape connected to the exposed FTO substrate. The electrolyte was 2 M potassium phosphate buffer (KP_i, pH≈7), with and without 0.5 M Na_2SO_3 as a hole scavenger. Potentials with respect to the reference electrode ($V_{Ag/AgCl}$) were applied by a potentiostat (EG&G PAR 273 A) and converted to the reversible hydrogen electrode scale (V_{RHE}) using the following equation

$$V_{RHE}(V) = V_{Ag/AgCl}(V) + 0.059 \times pH + V^0_{Ag/AgCl} \quad (7)$$

where $V^0_{Ag/AgCl}$ is the standard potential of the Ag/AgCl reference electrode (0.199 V at 25 °C). AM 1.5 photocurrent–voltage curves were measured under backside illumination using a solar simulator (WACOM WXS–50S–5 H, class AAA) with a scan rate of 25 mV s^{-1}.

Supporting Information

Supporting Information is available from the Wiley Online Library or from the author.

Acknowledgements

S.S. and N.W. would like to gratefully acknowledge the Thailand Science Research and Innovation (TSRI), formerly known as Thailand Research Fund (TRF) for the Royal Golden Jubilee (RGJ) Ph.D. Program (Grant No. PHD/0166/2557) and the Research Career Development Grant (Research Scholar Award; RSA5980035), the Program Management Unit for Human Resources & Institutional Development, Research and Innovation, Office of National Higher Education Science Research and Innovation Policy Council (NXPO) (Grant Number B16F640001), the Center of Excellence in Materials Science and Technology, Chiang Mai University. F.F.A. also thanks the RGJ Ph.D. program that allowed S.S. to visit and perform the research work at HZB. The authors also thank Dr. Zhibin Luo for his initial assistance with the spray pyrolysis setup and Qinthar A. Audiawarman for her assistance with the UV–vis spectroscopy measurements.

Open access funding enabled and organized by Projekt DEAL.

Conflict of Interest

The authors declare no conflict of interest.

Data Availability Statement

The data that support the findings of this study are available from the corresponding authors upon reasonable request.

Keywords

$BiVO_4$, carrier mobility, Gd doping, photoelectrochemical water splitting, time-resolved microwave conductivity

Received: April 9, 2021
Revised: June 4, 2021
Published online: July 7, 2021

[1] W.A. Smith, *Photoelectrochemical Solar Fuel Production* (Eds: S. Giménez, J. Bisquert), Springer, Cham, Switzerland **2016**.
[2] H. Pan, *Renew. Sust. Energ. Rev.* **2016**, *57*, 584.
[3] F. F. Abdi, S. P. Berglund, *J. Phys. D: Appl. Phys.* **2017**, *50*, 193002.
[4] A. Kudo, K. Omori, H. Kato, *J. Am. Chem. Soc.* **1999**, *121*, 11459.
[5] S. Tokunaga, H. Kato, A. Kudo, *Chem. Mater.* **2001**, *13*, 4624.
[6] C. Martinez Suarez, S. Hernández, N. Russo, *Appl. Catal., A* **2015**, *504*, 158.
[7] F. F. Abdi, R. van de Krol, *J. Phys. Chem. C* **2012**, *116*, 9398.
[8] F. F. Abdi, T. J. Savenije, M. M. May, B. Dam, R. van de Krol, *J. Phys. Chem. Lett.* **2013**, *4*, 2752.
[9] Y. Liang, T. Tsubota, L. P. A. Mooij, R. van de Krol, *J. Phys. Chem. C* **2011**, *115*, 17594.
[10] B. Zhang, H. Zhang, Z. Wang, X. Zhang, X. Qin, Y. Dai, Y. Liu, P. Wang, Y. Li, B. Huang, *Appl. Catal., B* **2017**, *211*, 258.
[11] A. Kudo, Y. Miseki, *Chem. Soc. Rev.* **2009**, *38*, 253.
[12] Y. Park, D. Kang, K.-S. Choi, *Phys. Chem. Chem. Phys.* **2014**, *16*, 1238.
[13] R. P. Antony, P. S. Bassi, F. F. Abdi, S. Y. Chiam, Y. Ren, J. Barber, J. S. C. Loo, L. H. Wong, *Electrochim. Acta* **2016**, *211*, 173.
[14] M. Rohloff, B. Anke, S. Zhang, U. Gernert, C. Scheu, M. Lerch, A. Fischer, *Sustain. Energy Fuels* **2017**, *1*, 1830.
[15] F. F. Abdi, N. Firet, *ChemCatChem* **2013**, *5*, 490.
[16] X. Zhao, J. Hu, S. Chen, Z. Chen, *Phys. Chem. Chem. Phys.* **2018**, *20*, 13637.
[17] S. P. Berglund, A. J. E. Rettie, S. Hoang, C. B. Mullins, *Phys. Chem. Chem. Phys.* **2012**, *14*, 7065.
[18] H. He, S. P. Berglund, A. J. E. Rettie, W. D. Chemelewski, P. Xiao, Y. Zhang, C. B. Mullins, *J. Mater. Chem. A* **2014**, *2*, 9371.
[19] M. Tayebi, B.-K. Lee, *Catal. Today* **2021**, *361*, 183.
[20] F. F. Abdi, L. Han, A. H. M. Smets, M. Zeman, B. Dam, R. van de Krol, *Nat. Commun.* **2013**, *4*, 2195.
[21] L. Han, F. F. Abdi, *ChemSusChem* **2014**, *7*, 2832.
[22] R. P. Antony, M. Zhang, K. Zhou, S. C. J. Loo, J. Barber, L. H. Wong, *ACS Omega* **2018**, *3*, 2724.
[23] X. Zhong, H. He, M. Yang, G. Ke, Z. Zhao, F. Dong, B. Wang, Y. Chen, X. Shi, Y. Zhou, *J. Mater. Chem. A* **2018**, *6*, 10456.
[24] G. V. Govindaraju, J. M. Morbec, G. A. Galli, K.-S. Choi, *J. Phys. Chem. C* **2018**, *122*, 19416.
[25] H. Xu, C. Wu, H. Li, J. Chu, G. Sun, Y. Xu, Y. Yan, *Appl. Surf. Sci.* **2009**, *256*, 597.
[26] Y. Luo, G. Tan, G. Dong, H. Ren, A. Xia, *Appl. Surf. Sci.* **2016**, *364*, 156.
[27] J. H. Baek, T. M. Gill, H. Abroshan, S. Park, X. Shi, J. Nørskov, H. S. Jung, S. Siahrostami, X. Zheng, *ACS Energy Lett.* **2019**, *4*, 720.
[28] P. F. Newhouse, D. Guevarra, M. Umehara, S. E. Reyes–Lillo, L. Zhou, D. A. Boyd, S. K. Suram, J. K. Cooper, J. A. Haber, J. B. Neaton, J. M. Gregoire, *Energy Environ. Sci.* **2018**, *11*, 2444.
[29] P. F. Newhouse, D. Guevarra, M. Umehara, D. A. Boyd, L. Zhou, J. K. Cooper, J. A. Haber, J. M. Gregoire, *Chem. Commun.* **2019**, *55*, 489.
[30] T. W. Kim, K.-S. Choi, *Science* **2014**, *343*, 990.
[31] T. H. Jeon, W. Choi, H. Park, *Phys. Chem. Chem. Phys.* **2011**, *13*, 21392.
[32] L. Cai, J. Zhao, H. Li, J. Park, I. S. Cho, H. S. Han, X. Zheng, *ACS Energy Lett.* **2016**, *1*, 624.
[33] L. Xia, J. Li, J. Bai, L. Li, S. Chen, B. Zhou, *Nano–Micro Lett.* **2017**, *10*, 11.
[34] L. Yang, Y. Xiong, W. Guo, J. Guo, D. Gao, Y. Zhang, P. Xiao, *Electrochim. Acta* **2017**, *256*, 268.
[35] H. L. Tan, F. F. Abdi, Y. H. Ng, *Chem. Soc. Rev.* **2019**, *48*, 1255.
[36] R. Irani, I. Y. Ahmet, J.-W. Jang, S. P. Berglund, P. Plate, C. Höhn, R. Böttger, S. W. Schmitt, C. Dubourdieu, S. Lardhi, L. Cavallo, M. Harb, P. Bogdanoff, R. van de Krol, F. F. Abdi, *Sol. RRL* **2020**, *4*, 1900290.
[37] T. J. Savenije, A. J. Ferguson, N. Kopidakis, G. Rumbles, *J. Phys. Chem. C* **2013**, *117*, 24085.
[38] M. Lamers, S. Fiechter, D. Friedrich, F. F. Abdi, R. van de Krol, *J. Mater. Chem. A* **2018**, *6*, 18694.
[39] M. Kölbach, H. Hempel, K. Harbauer, M. Schleuning, A. Petsiuk, K. Höflich, V. Deinhart, D. Friedrich, R. Eichberger, F. F. Abdi, R. van de Krol, *ACS Appl. Energy Mater.* **2020**, *3*, 4320.
[40] Y. Park, K. J. McDonald, K.-S. Choi, *Chem. Soc. Rev.* **2013**, *42*, 2321.
[41] R. D. Shannon, *Acta Crystallogr. A* **1976**, *32*, 751.
[42] X. Luo, G. Zhu, J. Peng, X. Wei, M. Hojamberdiev, L. Jin, P. Liu, *Appl. Surf. Sci.* **2015**, *351*, 260.
[43] M. Gotić, S. Musić, M. Ivanda, M. Šoufek, S. Popović, *J. Mol. Struct.* **2005**, *744–747*, 535.
[44] D. Zhou, L.-X. Pang, H. Wang, J. Guo, X. Yao, C. A. Randall, *J. Mater. Chem.* **2011**, *21*, 18412.
[45] F. D. Hardcastle, I. E. Wachs, *J. Phys. Chem.* **1991**, *95*, 5031.
[46] F. D. Hardcastle, I. E. Wachs, H. Eckert, D. A. Jefferson, *J. Solid State Chem.* **1991**, *90*, 194.
[47] A. W. Sleight, H. Y. Chen, A. Ferretti, D. E. Cox, *Mater. Res. Bull.* **1979**, *14*, 1571.
[48] S. R. M. Thalluri, C. Martinez–Suarez, A. Virga, N. Russo, G. Saracco, *Int. J. Chem. Eng. Appl.* **2013**, *4*, 305.
[49] J. Yu, A. Kudo, *Adv. Funct. Mater.* **2006**, *16*, 2163.
[50] R. van de Krol, *Photoelectrochemical Hydrogen Production* (Eds: R. van de Krol, M. Grätzel) *102*, Springer, New York **2012**.
[51] F. F. Abdi, N. Firet, A. Dabirian, R. van de Krol, in *MRS Online Proc. Libr.* **2012**, p. 1446.
[52] I. Y. Ahmet, Y. Ma, J.-W. Jang, T. Henschel, B. Stannowski, T. Lopes, A. Vilanova, A. Mendes, F. F. Abdi, R. van de Krol, *Sustain. Energy Fuels* **2019**, *3*, 2366.
[53] F. Wang, A. Chemseddine, F. F. Abdi, R. van de Krol, S. P. Berglund, *J. Mater. Chem. A* **2017**, *5*, 12838.
[54] J.-W. Jang, D. Friedrich, S. Müller, M. Lamers, H. Hempel, S. Lardhi, Z. Cao, M. Harb, L. Cavallo, R. Heller, R. Eichberger, R. van de Krol, F. F. Abdi, *Adv. Energy Mater.* **2017**, *7*, 1701536.